

Synthesis, Structural, and Spectroscopic Characterization and Reactivities of Mononuclear Cobalt(III)–Peroxo Complexes

Jaeheung Cho,[†] Ritimukta Sarangi,[‡] Hye Yeon Kang,[†] Jung Yoon Lee,[†]
Minoru Kubo,[§] Takashi Ogura,[§] Edward I. Solomon,^{‡,||} and Wonwoo Nam^{*,†}

Department of Bioinspired Science, Department of Chemistry and Nano Science, Center for Biomimetic Systems, Ewha Womans University, Seoul 120-750, Korea, Stanford Synchrotron Radiation Lightsource, SLAC National Accelerator Laboratory, Menlo Park, California 94025, United States, Picobiology Institute, Graduate School of Life Science, University of Hyogo, Hyogo 678-1297, Japan, and Department of Chemistry, Stanford University, Stanford, California 94305, United States

Received August 10, 2010; E-mail: wwnam@ewha.ac.kr

Abstract: Metal–dioxygen adducts are key intermediates detected in the catalytic cycles of dioxygen activation by metalloenzymes and biomimetic compounds. In this study, mononuclear cobalt(III)–peroxo complexes bearing tetraazamacrocyclic ligands, [Co(12-TMC)(O₂)]⁺ and [Co(13-TMC)(O₂)]⁺, were synthesized by reacting [Co(12-TMC)(CH₃CN)]²⁺ and [Co(13-TMC)(CH₃CN)]²⁺, respectively, with H₂O₂ in the presence of triethylamine. The mononuclear cobalt(III)–peroxo intermediates were isolated and characterized by various spectroscopic techniques and X-ray crystallography, and the structural and spectroscopic characterization demonstrated unambiguously that the peroxo ligand is bound in a side-on η^2 fashion. The O–O bond stretching frequency of [Co(12-TMC)(O₂)]⁺ and [Co(13-TMC)(O₂)]⁺ was determined to be 902 cm^{−1} by resonance Raman spectroscopy. The structural properties of the CoO₂ core in both complexes are nearly identical; the O–O bond distances of [Co(12-TMC)(O₂)]⁺ and [Co(13-TMC)(O₂)]⁺ were 1.4389(17) Å and 1.438(6) Å, respectively. The cobalt(III)–peroxo complexes showed reactivities in the oxidation of aldehydes and O₂-transfer reactions. In the aldehyde oxidation reactions, the nucleophilic reactivity of the cobalt–peroxo complexes was significantly dependent on the ring size of the macrocyclic ligands, with the reactivity of [Co(13-TMC)(O₂)]⁺ > [Co(12-TMC)(O₂)]⁺. In the O₂-transfer reactions, the cobalt(III)–peroxo complexes transferred the bound peroxo group to a manganese(II) complex, affording the corresponding cobalt(II) and manganese(III)–peroxo complexes. The reactivity of the cobalt–peroxo complexes in O₂-transfer was also significantly dependent on the ring size of tetraazamacrocycles, and the reactivity order in the O₂-transfer reactions was the same as that observed in the aldehyde oxidation reactions.

1. Introduction

Mononuclear metal–dioxygen adducts, M–O₂, are generated as key intermediates in the catalytic cycles of dioxygen activation by metalloenzymes, including heme and nonheme iron and copper enzymes.¹ As chemical models of the enzymes, a number of metal–O₂ complexes have been synthesized and characterized with various spectroscopic techniques and X-ray crystallography, and their reactivities have been extensively investigated in electrophilic and nucleophilic oxidation reactions.^{2–6} For example, heme and nonheme iron(III)–O₂ complexes were synthesized as chemical models of Cytochrome P450 aromatases and Rieske dioxygenases, respectively, and have shown reac-

tivities in nucleophilic reactions such as aldehyde deformylation.⁴ Mononuclear Cu–O₂ complexes have been synthesized as chemical models of copper-containing enzymes, such as peptidylglycine α -hydroxylating monooxygenase (PHM) and dopamine β -monooxygenase (D β M),⁵ and their reactivities have been investigated in electrophilic reactions.⁶

The chemistry of cobalt–O₂ complexes bearing salen, porphyrin, and tetraazamacrocyclic ligands has been extensively investigated as chemical models of dioxygen-carrying proteins, such as hemoglobin and myoglobin,⁷ and as active

[†] Ewha Womans University.[‡] SLAC National Accelerator Laboratory.[§] University of Hyogo.^{||} Stanford University.

(1) (a) *Cytochrome P450: Structure, Mechanism, and Biochemistry*, 3rd ed.; Ortiz de Montellano, P. R., Ed.; Kluwer Academic/Plenum Publishers: New York, 2005. (b) *Comprehensive Coordination Chemistry II*; Que, L., Jr., Tolman, W. B., Eds.; Elsevier: Oxford, 2004. (c) *Biomimetic Oxidations Catalyzed by Transition Metal Complexes*; Meunier, B., Ed.; Imperial College Press: London, 2000; Vol. 8.

(2) (a) Sen, K.; Hackett, J. C. *J. Am. Chem. Soc.* **2010**, *132*, 10293–10305. (b) Shyadehi, A. Z.; Lamb, D. C.; Kelly, S. L.; Kelly, D. E.; Schunck, W. H.; Wright, J. N.; Corina, D.; Akhtar, M. *J. Biol. Chem.* **1996**, *271*, 12445–12450. (c) Vaz, A. D.; Pernecky, S. J.; Raner, G. M.; Coon, M. J. *Proc. Natl. Acad. Sci. U.S.A.* **1996**, *93*, 4644–4648. (d) Roberts, E. S.; Vaz, A. D. N.; Coon, M. J. *Proc. Natl. Acad. Sci. U.S.A.* **1991**, *88*, 8963–8966. (3) (a) Valentine, J. S. *Chem. Rev.* **1973**, *73*, 235–245. (b) Basolo, F.; Hoffman, B. M.; Ibers, J. A. *Acc. Chem. Res.* **1975**, *8*, 384–392. (c) Vaska, L. *Acc. Chem. Res.* **1976**, *9*, 175–183. (d) Klotz, I. M.; Kurtz, D. M., Jr. *Chem. Rev.* **1994**, *94*, 567–568, and review articles in the special issue. (e) Bakac, A. *Coord. Chem. Rev.* **2006**, *250*, 2046–2058. (f) Nam, W. *Acc. Chem. Res.* **2007**, *40*, 465, and review articles in the special issue.

oxidants in the oxidation of organic substrates.⁸ As a result, structural and spectroscopic characterization of the cobalt–O₂ complexes has been well established in the 1970s. The structural analysis of the cobalt–O₂ complexes by X-ray crystallography revealed that the O₂ group in the intermediates has superoxo character with an end-on (η^1) binding mode, Co(III)–(O₂[–]).^{7c,9} Mononuclear cobalt–O₂ complexes with a side-on (η^2) cobalt(III)–peroxo moiety, Co(III)–(O₂^{2–}), have also been reported,¹⁰ such as [Co(2=phos)₂(O₂)]⁺ (2=phos = *cis*-[(C₆H₅)₂PCH=CHP(C₆H₅)₂]),^{10a} Co(Tp')(O₂) (Tp' = hydridotris(3-*tert*-butyl-5-methylpyrazolyl)borate),^{10b} [Co(tmen)₂(O₂)]⁺ (tmen = tetramethylethylenediamine),^{10c} [Co(TIMEN^{xy}l)(O₂)]⁺ (TIMEN^{xy}l = tris[2-(3-xylenylimidazol-2-ylidene)ethyl]amine).^{10d} The oxidation of organic substrates, such as phenols and olefins, by Co(II) Schiff base complexes has also been extensively investigated under aerobic, catalytic conditions.^{8,11} In the oxidation reactions, end-on cobalt(III)–superoxo complexes, Co(III)–(O₂[–]), have been proposed as active oxidants that abstract a hydrogen atom (H-atom) from weak O–H or C–H bonds of substrates.¹¹

Very recently, we reported the crystal structure and spectroscopic properties of a mononuclear side-on nickel(III)–peroxo complex bearing a macrocyclic ligand, [Ni(12-TMC)(O₂)]⁺ (12-TMC = 1,4,7,10-tetramethyl-1,4,7,10-tetraazacyclododecane), and an O₂-transfer reaction of the intermediate (i.e., intermolecular O₂-transfer reaction).^{12a} In that study, we demonstrated that the geometric and electronic structures and reactivities of the Ni–O₂ complexes are markedly affected by supporting ligands,¹² as shown in the chemistry of mononuclear Cu–O₂ complexes.¹³ Crystal structures of other metal–O₂ complexes bearing tetraazamacrocyclic ligands, such as [Mn(14-TMC)(O₂)]⁺ (14-TMC = 1,4,8,11-tetramethyl-1,4,8,11-tetraazacyclotetradecane), [Mn(13-TMC)(O₂)]⁺ (13-TMC = 1,4,7,10-tetramethyl-1,4,7,10-tetraazacyclotridecane), and [Cr(14-TMC)(O₂)(Cl)]⁺, have also been reported along with their reactivities in aldehyde deformation and C–H bond activation reactions.^{14,15} Herein we report the synthesis, structural and spectroscopic characterization, and reactivities of side-on cobalt(III)–peroxo complexes bearing tetraazamacrocyclic ligands, [Co(12-TMC)(O₂)]⁺ (**2**) and [Co(13-TMC)(O₂)]⁺ (**4**).¹⁶ We have also shown that reactivities of metal–peroxo intermediates in O₂-transfer and oxidative nucleophilic reactions are markedly affected by the central metal ions and the ring size of the macrocyclic ligands.

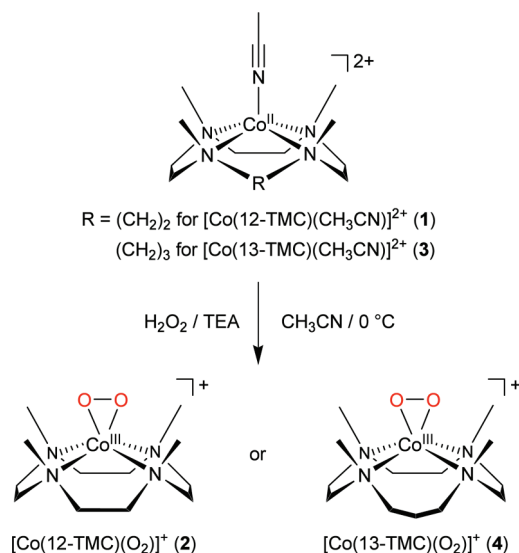
2. Results and Discussion

2.1. Synthesis of Co–O₂ Complexes. Synthetic procedures for cobalt(III)–peroxo complexes are depicted in Scheme 1. The starting materials, [Co(12-TMC)(CH₃CN)]²⁺ (**1**) and [Co(13-TMC)(CH₃CN)]²⁺ (**3**), were prepared by reacting Co(ClO₄)₂·6H₂O with the corresponding 12-TMC and 13-TMC ligands, respectively. The cobalt(III)–peroxo complexes were then synthesized as follows: Addition of 5 equiv of H₂O₂ to a reaction solution containing **1** and 2 equiv of triethylamine (TEA) in CH₃CN at 0 °C afforded a purple intermediate, [Co(12-TMC)(O₂)]⁺ (**2**). **2** was then isolated at a temperature below –20 °C. Similarly, [Co(13-TMC)(O₂)]⁺ (**4**) was obtained by reacting **3** with 5 equiv of H₂O₂ in the presence of 2 equiv of TEA in CH₃CN at 0 °C and isolated at a temperature below –40 °C. The intermediates, **2** and **4**, persisted for several days

- (4) (a) Wertz, D. L.; Valentine, J. S. *Struct. Bonding (Berlin)* **2000**, 97, 37–60. (b) Gibson, D. T.; Parales, R. E. *Curr. Opin. Biotechnol.* **2000**, 11, 236–243. (c) Wertz, D. L.; Sisemore, M. F.; Selke, M.; Driscoll, J.; Valentine, J. S. *J. Am. Chem. Soc.* **1998**, 120, 5331–5332. (d) Goto, Y.; Wada, S.; Morishima, I.; Watanabe, Y. *J. Inorg. Biochem.* **1998**, 69, 241–247. (e) Hashimoto, K.; Nagatomo, S.; Fujinami, S.; Furutachi, H.; Ogo, S.; Suzuki, M.; Uehara, A.; Maeda, Y.; Watanabe, Y.; Kitagawa, T. *Angew. Chem., Int. Ed.* **2002**, 41, 1202–1205. (f) Annaraj, J.; Suh, Y.; Seo, M. S.; Kim, S. O.; Nam, W. *Chem. Commun.* **2005**, 4529–4531. (g) Kovaleva, E. G.; Lipscomb, J. D. *Science* **2007**, 316, 453–457.
- (5) (a) Prigge, S. T.; Eipper, B. A.; Mains, R. E.; Amzel, L. M. *Science* **2004**, 304, 864–867. (b) Mirica, L. M.; Ottenwaelde, X.; Stack, T. D. P. *Chem. Rev.* **2004**, 104, 1013–1045. (c) Lewis, E. A.; Tolman, W. B. *Chem. Rev.* **2004**, 104, 1047–1076. (d) Hatcher, L. Q.; Karlin, K. D. *J. Biol. Inorg. Chem.* **2004**, 9, 669–683. (e) Chen, P.; Solomon, E. I. *Proc. Natl. Acad. Sci. U.S.A.* **2004**, 101, 13105–13110. (f) Chen, P.; Solomon, E. I. *J. Am. Chem. Soc.* **2004**, 126, 4991–5000. (g) Klinman, J. P. *J. Biol. Chem.* **2006**, 281, 3013–3016. (h) Itoh, S. *Curr. Opin. Chem. Biol.* **2006**, 10, 115–122. (i) Cramer, C. J.; Tolman, W. B. *Acc. Chem. Res.* **2007**, 40, 601–608. (j) Rolff, M.; Tuzcek, F. *Angew. Chem., Int. Ed.* **2008**, 47, 2344–2347.
- (6) (a) Himes, R. A.; Karlin, K. D. *Curr. Opin. Chem. Biol.* **2009**, 13, 119–131. (b) Kunishita, A.; Kubo, M.; Sugimoto, H.; Ogura, T.; Sato, K.; Takui, T.; Itoh, S. *J. Am. Chem. Soc.* **2009**, 131, 2788–2789. (c) Maiti, D.; Lee, D.-H.; Gaoutchenova, K.; Würtele, C.; Holthausen, M. C.; Sarjeant, A. A. N.; Sundermeyer, J.; Schindler, S.; Karlin, K. D. *Angew. Chem., Int. Ed.* **2008**, 47, 82–85. (d) Fujii, T.; Yamaguchi, S.; Hirota, S.; Masuda, H. *Dalton Trans.* **2008**, 164–170. (e) Maiti, D.; Fry, H. C.; Woertink, J. S.; Vance, M. A.; Solomon, E. I.; Karlin, K. D. *J. Am. Chem. Soc.* **2007**, 129, 264–265.
- (7) (a) Hikichi, S.; Akita, M.; Moro-oka, Y. *Coord. Chem. Rev.* **2000**, 198, 61–87. (b) Busch, D. H.; Alcock, N. W. *Chem. Rev.* **1994**, 94, 585–623. (c) Smith, T. D.; Pilbrow, J. R. *Coord. Chem. Rev.* **1981**, 39, 295–383.
- (8) Bailey, C. L.; Drago, R. S. *Coord. Chem. Rev.* **1987**, 79, 321–332, and references therein.
- (9) (a) Busch, D. H.; Jackson, P. J.; Kojima, M.; Chmielewski, P.; Matsumoto, N.; Stevens, J. C.; Wu, W.; Nosco, D.; Herron, N.; Ye, N.; Warburton, P. R.; Masarwa, M.; Stephenson, N. A.; Christoph, G.; Alcock, N. W. *Inorg. Chem.* **1994**, 33, 910–923. (b) Schaefer, W. P.; Huie, B. T.; Kurilla, M. G.; Ealick, S. E. *Inorg. Chem.* **1980**, 19, 340–344.
- (10) (a) Terry, N. W.; Amma, E. L.; Vaska, L. *J. Am. Chem. Soc.* **1972**, 94, 653–655. (b) Egan, J. W., Jr.; Haggerty, B. S.; Rheingold, A. L.; Sendlinger, S. C.; Theopold, K. H. *J. Am. Chem. Soc.* **1990**, 112, 2445–2446. (c) Rahman, A. F. M. M.; Jackson, W. G.; Willis, A. C. *Inorg. Chem.* **2004**, 43, 7558–7560. (d) Hu, X.; Castro-Rodriguez, I.; Meyer, K. J. *J. Am. Chem. Soc.* **2004**, 126, 13464–13473.
- (11) (a) Zombeck, A.; Drago, R. S.; Corden, B. B.; Gaul, J. H. *J. Am. Chem. Soc.* **1981**, 103, 7580–7585. (b) Hamilton, D. E.; Drago, R. S.; Zombeck, A. *J. Am. Chem. Soc.* **1987**, 109, 374–379.

- (12) (a) Cho, J.; Sarangi, R.; Annaraj, J.; Kim, S. Y.; Kubo, M.; Ogura, T.; Solomon, E. I.; Nam, W. *Nat. Chem.* **2009**, 1, 568–572. (b) Kieber-Emmons, M. T.; Annaraj, J.; Seo, M. S.; Van Heuvelen, K. M.; Tosha, T.; Kitagawa, T.; Brunold, T. C.; Nam, W.; Riordan, C. G. *J. Am. Chem. Soc.* **2006**, 128, 14230–14231.
- (13) (a) Fujisawa, K.; Tanaka, M.; Moro-oka, Y.; Kitajima, N. *J. Am. Chem. Soc.* **1994**, 116, 12079–12080. (b) Spencer, D. J. E.; Aboelella, N. W.; Reynolds, A. M.; Holland, P. L.; Tolman, W. B. *J. Am. Chem. Soc.* **2002**, 124, 2108–2109. (c) Gherman, B. F.; Cramer, C. J. *Inorg. Chem.* **2004**, 43, 7281–7283. (d) Aboelella, N. W.; Kryatov, S. V.; Gherman, B. F.; Brennessel, W. W.; Young, V. G., Jr.; Sarangi, R.; Rybak-Akimova, E. V.; Hodgson, K. O.; Hedman, B.; Solomon, E. I.; Cramer, C. J.; Tolman, W. B. *J. Am. Chem. Soc.* **2004**, 126, 16896–16911. (e) Reynolds, A. M.; Gherman, B. F.; Cramer, C. J.; Tolman, W. B. *Inorg. Chem.* **2005**, 44, 6989–6997. (f) Sarangi, R.; Aboelella, N.; Fujisawa, K.; Tolman, W. B.; Hedman, B.; Hodgson, K. O.; Solomon, E. I. *J. Am. Chem. Soc.* **2006**, 128, 8286–8296. (g) Würtele, C.; Gaoutchenova, E.; Harms, K.; Holthausen, M. C.; Sundermeyer, J.; Schindler, S. *Angew. Chem., Int. Ed.* **2006**, 45, 3867–3869.
- (14) (a) Seo, M. S.; Kim, J. Y.; Annaraj, J.; Kim, Y.; Lee, Y.-M.; Kim, S.-J.; Kim, J.; Nam, W. *Angew. Chem., Int. Ed.* **2007**, 46, 377–380. (b) Annaraj, J.; Cho, J.; Lee, Y.-M.; Kim, S. Y.; Latifi, R.; de Visser, S. P.; Nam, W. *Angew. Chem., Int. Ed.* **2009**, 48, 4150–4153.
- (15) Cho, J.; Woo, J.; Nam, W. *J. Am. Chem. Soc.* **2010**, 132, 5958–5959.
- (16) Although the structure of [Co(14-TMC)(O₂)]⁺ was not available, we have reported the reactivity of [Co(14-TMC)(O₂)]⁺ in the deformylation of aldehydes: Jo, Y.; Annaraj, J.; Seo, M. S.; Lee, Y.-M.; Kim, S. Y.; Cho, J.; Nam, W. *J. Inorg. Biochem.* **2008**, 102, 2155–2159.

Scheme 1



at 0 °C. The greater thermal stability of **2** and **4** allowed us to use isolated cobalt–peroxo intermediates in spectroscopic and reactivity studies.

2.2. Structural and Spectroscopic Characterization. 2.2.1. X-ray Crystallography. Complexes **1–4** were successfully characterized by X-ray diffraction analyses. The molecular structures of the complex cations of **1–4** are shown in Figure 1 and Supporting Information (SI), Figure S1, and selected bond distances and angles are listed in Table 1 and Table S1 in the Supporting Information (SI). Complex **1** has a five-coordinate cobalt(II) ion with four nitrogens of the macrocyclic 12-TMC ligand in equatorial positions and one nitrogen of CH₃CN in an axial position (SI, Figure S1a), as found in a nickel(II) analog, [Ni(12-TMC)(CH₃CN)]²⁺.^{12a} Complex **3** has a coordination geometry similar to that of **1** (SI, Figure S1b). The average Co–N_{equatorial} bond distance of **3** (2.068 Å) is longer than that of **1** (1.988 Å), but the Co–N_{axial} bond distance of **3** (2.015 Å) is slightly shorter than that of **1** (2.036 Å).

The X-ray structures of **2** and **4** revealed a mononuclear side-on cobalt–O₂ complex in a distorted octahedral geometry arising from the triangular CoO₂ moiety with a small bite angle of 45.36(5)° for **2** and 45.16(12)° for **4** (Figure 1). The O–O bond lengths of 1.4389(17) Å for **2** and 1.438(4) Å for **4**, which are comparable to those in [Co(tmen)₂(O₂)]⁺ (1.457 Å) and [Co(TI-MEN^{xy}l)(O₂)]⁺ (1.429 Å),^{10c,d} are indicative of the peroxo character of the O₂ group,¹⁷ as assigned by resonance Raman data (vide infra). The average Co–O bond distance of **4** (1.856 Å) is slightly shorter than that of **2** (1.866 Å). Further, the O–O bond distances of **2** and **4** are longer than that of [Ni(12-

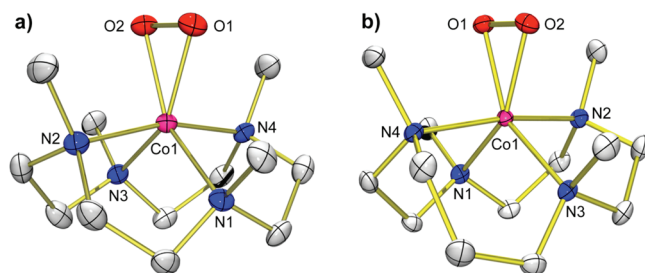


Figure 1. X-ray crystal structures of (a) [Co(12-TMC)(O₂)]⁺ (**2**) and (b) [Co(13-TMC)(O₂)]⁺ (**4**) with thermal ellipsoids drawn at the 30% probability level. Hydrogen atoms are omitted for clarity.

Table 1. Selected Bond Distances (Å) and Angles (deg) for **2**-(BPh₄)•CH₃CN and **4**-(ClO₄)•CH₃CN

	2 -(BPh ₄)•CH ₃ CN	4 -(ClO ₄)•CH ₃ CN
Co1–N1	1.9991(17)	1.995(3)
Co1–N2	2.0155(18)	2.017(3)
Co1–N3	1.9969(16)	2.078(3)
Co1–N4	2.0249(18)	2.037(3)
Co1–O1	1.8737(12)	1.846(2)
Co1–O2	1.8575(13)	1.864(3)
O1–O2	1.4389(17)	1.438(4)
N1–Co1–N2	85.93(8)	85.67(12)
N1–Co1–N3	110.88(7)	108.84(13)
N1–Co1–N4	85.96(8)	84.77(13)
N2–Co1–N3	86.28(7)	86.05(12)
N2–Co1–N4	165.09(7)	170.10(12)
N3–Co1–N4	84.94(8)	94.58(12)
O1–Co1–O2	45.36(5)	45.61(12)
Co1–O1–O2	66.72(7)	67.85(14)
Co1–O2–O1	67.91(8)	66.54(14)

TMC)(O₂)]⁺ (1.386 Å), whereas the average Co–O bond distances of **2** (1.866 Å) and **4** (1.856 Å) are shorter than the average Ni–O bond distance of [Ni(12-TMC)(O₂)]⁺ (1.889 Å).^{12a} Finally, all four *N*-methyl groups of the 12-TMC and 13-TMC ligands point toward the peroxo group, as observed in other metal(III)–peroxo complexes bearing tetraazamacrocyclic ligands, such as [Ni(12-TMC)(O₂)]⁺,^{12a} [Mn(14-TMC)(O₂)]⁺,^{14a} and [Mn(13-TMC)(O₂)]⁺.^{14b}

2.2.2. Co K-Edge X-ray Absorption and EXAFS. The normalized Co K-edge X-ray absorption data for **2** and **4** are presented in SI, Figure S2. The inset shows the pre-edge transition, which is the result of an electric dipole forbidden, quadrupole allowed 1s→3d transition. The pre-edge energy position dominantly reflects the ligand-field strength at the absorbing metal center. The pre-edge transition for both **2** and **4** occurs at ~7710.1 eV. The intense step-function-like feature to higher energy (~7712 to 7728 eV) is the rising edge, which occurs due to dipole-allowed 1s→4p+continuum transitions. The rising edge inflection energy reflects the charge at the absorbing metal center. This inflection point occurs at ~7721.0 eV for both **2** and **4**, an energy typical for Co(III) systems.¹⁸ The similarity in the pre-edge energy and the rising edge inflection points indicates that **2** and **4** are both Co(III)–O₂^{2–} complexes.

Co K-edge extended X-ray absorption fine structure (EXAFS) data were collected on **2** and **4** to evaluate the geometric structure of the O₂ bound adducts of **1** and **3** in solution and compare them to the crystal structures. The *k*³ weighted Co K-edge EXAFS data (SI, Figure S3, inset), non-phase-shift-corrected Fourier transform (*k* = 2–14 Å^{–1}) and the corresponding *FEFF* fits for **2** and for **4** are shown in SI, Figure S3a and S3b, respectively. Numerical fits are presented in Table S2. *FEFF* fits to the data for **2** are consistent with 2 Co–O interactions at 1.85 Å and 4 Co–N interactions at 1.99 Å. The second shell for **2** was fit with 8 Co–C single-scattering and 24 Co–C–N multiple-scattering components from the 12-TMC ligand backbone carbons. *FEFF* fits to the data for **4** resulted in structural parameters similar to those for **2**. The first shell was fit with 2 Co–O contributions at 1.85 Å and 4 Co–N contributions at 2.0 Å. The second shell was fit with 8 Co–C single-scattering and 24 Co–C–N multiple-scattering compo-

(17) Cramer, C. J.; Tolman, W. B.; Theopold, K. H.; Rheingold, A. L. *Proc. Natl. Acad. Sci. U.S.A.* **2003**, *100*, 3635–3640.

(18) Fujita, E.; Furenli, L. R.; Renner, M. W. *J. Am. Chem. Soc.* **1997**, *119*, 4549–4550.

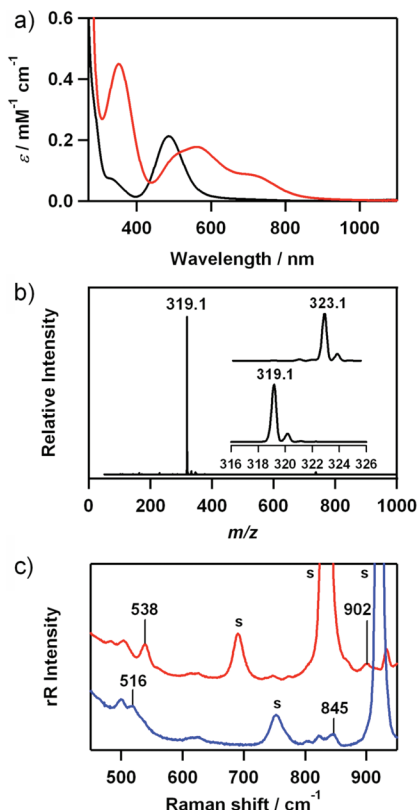


Figure 2. (a) UV-vis spectra of $[\text{Co}(\text{12-TMC})(\text{CH}_3\text{CN})]^{2+}$ (**1**) (black) and $[\text{Co}(\text{12-TMC})(\text{O}_2)]^+$ (**2**) (red) in CH_3CN at 0°C . (b) ESI-MS of **2** in CH_3CN at 0°C . Insets show the observed isotope distribution patterns for $[\text{Co}(\text{12-TMC})(^{16}\text{O}_2)]^+$ at m/z 319.1 and $[\text{Co}(\text{12-TMC})(^{18}\text{O}_2)]^+$ at m/z 323.1. (c) Resonance Raman spectra of **2** (32 mM) obtained upon excitation at 442 nm at 0°C ; in situ generated $2\text{-}^{16}\text{O}_2$ (red line) and $2\text{-}^{18}\text{O}_2$ (blue line) were recorded in CD_3CN and CH_3CN , respectively, owing to a significant overlap with intense solvent bands. The peaks marked with “s” are ascribed to acetonitrile and d_3 -acetonitrile solvents. See SI, Figure S4 for resonance Raman spectra of **2** recorded under various conditions.

nents from the 13-TMC ligand backbone carbons. The additional carbon atom in the 13-TMC ring is at a longer distance than the rest of the ring carbon atoms and does not contribute to the second shell single and multiple scattering. The similarity in the EXAFS fit parameters for **2** and **4** and the resulting structural parameters demonstrate that the solution structure of both **2** and **4** are in agreement with the crystal structure and both the species are mononuclear species with O_2 bound in a side-on (η^2) fashion to the Co center.

2.2.3. Spectroscopic Characterization. 2.2.3.1. $[\text{Co}(\text{12-TMC})(\text{O}_2)]^+$ (2**).** The electronic spectrum of **2** shows distinct absorption bands at 350 ($\epsilon = 450 \text{ M}^{-1} \text{ cm}^{-1}$) and 560 nm ($\epsilon = 180 \text{ M}^{-1} \text{ cm}^{-1}$) and shoulders at ~ 500 ($\epsilon = 150 \text{ M}^{-1} \text{ cm}^{-1}$) and ~ 710 nm ($\epsilon = 90 \text{ M}^{-1} \text{ cm}^{-1}$) (Figure 2a). The electrospray ionization mass spectrum (ESI-MS) of **2** exhibits a prominent signal at m/z 319.1 (Figure 2b), whose mass and isotope distribution pattern correspond to $[\text{Co}(\text{12-TMC})(\text{O}_2)]^+$ (calculated m/z 319.2) (Figure 2b, inset). When the reaction was carried out with isotopically labeled $\text{H}_2^{18}\text{O}_2$, a mass peak corresponding to $[\text{Co}(\text{12-TMC})(^{18}\text{O}_2)]^+$ appeared at an m/z of 323.1 (calculated m/z 323.2) (Figure 2b, inset). The observation of the 4-mass-unit upshift upon the substitution of ^{16}O with ^{18}O indicates that **2** contains an O_2 unit.

The resonance Raman spectrum of **2** obtained upon 442-nm excitation in CD_3CN at 0°C exhibits two isotopically sensitive bands at 902 and 538 cm^{-1} that shift to 845 and 516 cm^{-1} ,

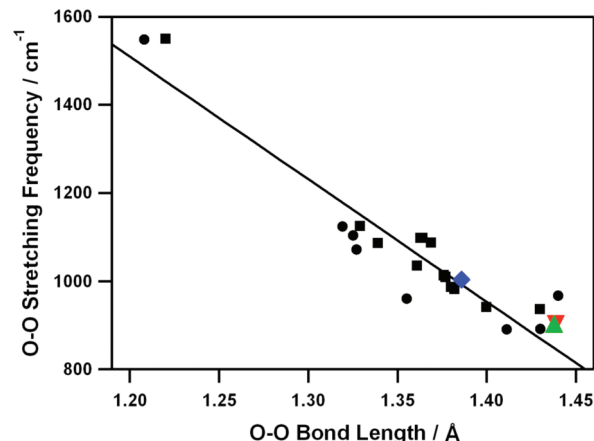


Figure 3. Plot of the O–O stretching frequency (cm^{-1}) vs the O–O bond distance (\AA) for side-on metal– O_2 complexes. Circles represent experimental data points, and squares represent theoretical ones taken from ref 17. The solid line represents a least-squares linear fit of the experimental and theoretical data. Data points for $[\text{Co}(\text{12-TMC})(\text{O}_2)]^+$ (**2**) (▼), $[\text{Co}(\text{13-TMC})(\text{O}_2)]^+$ (**4**) (▲), and $[\text{Ni}(\text{12-TMC})(\text{O}_2)]^+$ (◆) are included in the diagram.

respectively, in samples of **2** prepared with $\text{H}_2^{18}\text{O}_2$ in CH_3CN (Figure 2c and SI, Figure S4). The higher energy feature (902 cm^{-1}) with a $^{16}\Delta\text{--}^{18}\Delta$ value of 57 cm^{-1} ($^{16}\Delta\text{--}^{18}\Delta$ (calcd) = 51 cm^{-1}) is ascribed to the O–O stretching vibration of the peroxo ligand, and the lower-energy feature (538 cm^{-1}) is assigned to the Co–O stretching vibration ($^{16}\Delta\text{--}^{18}\Delta = 22 \text{ cm}^{-1}$; $^{16}\Delta\text{--}^{18}\Delta$ (calcd) = 24 cm^{-1}).¹⁹ In addition, we have observed a good correlation between the O–O stretching frequency and the O–O bond length in **2** (Figure 3).¹⁷

The X-band EPR spectrum of the starting complex, $[\text{Co}(\text{12-TMC})(\text{CH}_3\text{CN})]^{2+}$ (**1**), at 4.3 K contains features at $g_{\perp} = 2.31$ and $g_{\parallel} \approx 2.07$, which are typical for a low-spin ($S = 1/2$) cobalt(II) complex (SI, Figure S5). The EPR spectrum of **2** is silent at 4.3 K (SI, Figure S5), suggesting that **2** is either a low-spin ($S = 0$) or an integer spin ($S = 1, 2$) cobalt(III) d^6 species. The ^1H NMR and COSY spectra of **2** recorded in d_3 -acetonitrile at -40°C show sharp features in the 0–10 ppm region (SI, Figure S6), indicating that **2** is, in fact, a low-spin ($S = 0$) cobalt(III) d^6 species at -40°C .

2.2.3.2. $[\text{Co}(\text{13-TMC})(\text{O}_2)]^+$ (4**).** Spectroscopic properties of **4** are similar to those of **2**. The electronic spectrum of **4** shows distinct absorption bands at 348 ($\epsilon = 620 \text{ M}^{-1} \text{ cm}^{-1}$) and 562 nm ($\epsilon = 210 \text{ M}^{-1} \text{ cm}^{-1}$) and shoulders at ~ 500 ($\epsilon = 170 \text{ M}^{-1} \text{ cm}^{-1}$) and ~ 710 nm ($\epsilon = 100 \text{ M}^{-1} \text{ cm}^{-1}$) (Figure 4a). The ESI-MS of **4** exhibits a prominent mass signal at m/z 333.1 (Figure 4b), whose mass and isotope distribution pattern correspond to those of $[\text{Co}(\text{13-TMC})(\text{O}_2)]^+$ (calculated m/z 333.2), with the expected 4-mass-unit upshift upon the substitution of ^{16}O by ^{18}O (Figure 4b, inset).

The resonance Raman spectrum of **4**, obtained upon 442-nm excitation in CD_3CN at 0°C , exhibits two isotopically sensitive bands at 902 and 542 cm^{-1} that shift to 846 and 520 cm^{-1} , respectively, in samples of **4** prepared with $\text{H}_2^{18}\text{O}_2$ in CH_3CN (Figure 4c and SI, Figure S7). The higher energy feature (902 cm^{-1}) with a $^{16}\Delta\text{--}^{18}\Delta$ value of 56 cm^{-1} ($^{16}\Delta\text{--}^{18}\Delta$ (calcd) = 51 cm^{-1}) is ascribed to the O–O stretching vibration of the peroxo ligand, and the lower energy feature (542 cm^{-1}) is assigned to the Co–O stretching

(19) Girerd, J.-J.; Banse, F.; Simaan, A. *J. Struct. Bonding (Berlin)* **2000**, 97, 145–177.

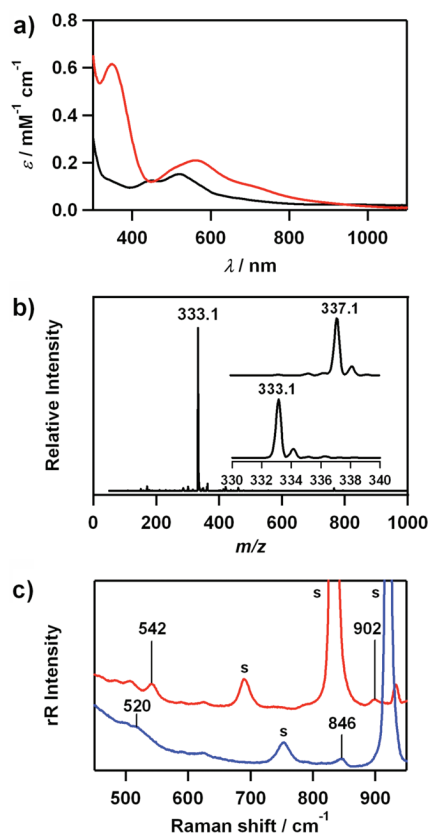


Figure 4. (a) UV–vis spectra of $[\text{Co}(\text{13-TMC})(\text{CH}_3\text{CN})]^{2+}$ (**3**) (black) and $[\text{Co}(\text{13-TMC})(\text{O}_2)]^+$ (**4**) (red) in CH_3CN at 0°C . (b) ESI-MS of **4** in CH_3CN at 0°C . Insets show the observed isotope distribution patterns for $[\text{Co}(\text{13-TMC})(^{16}\text{O}_2)]^+$ at m/z 333.1 and $[\text{Co}(\text{13-TMC})(^{18}\text{O}_2)]^+$ at m/z 337.1. (c) Resonance Raman spectra of **4** (32 mM) obtained upon excitation at 442 nm at 0°C ; in situ generated **4**- $^{16}\text{O}_2$ (red line) and **4**- $^{18}\text{O}_2$ (blue line) were recorded in CD_3CN and CH_3CN , respectively, owing to a significant overlap with intense solvent bands. The peaks marked with “s” are ascribed to acetonitrile and d_3 -acetonitrile solvents. See SI, Figure S7 for resonance Raman spectra of **4** recorded under various conditions.

vibration ($^{16}\Delta\text{--}^{18}\Delta = 22\text{ cm}^{-1}$; $^{16}\Delta\text{--}^{18}\Delta$ (calcd) = 24 cm^{-1}).¹⁹ Like **2**, the relatively low O–O frequency is consistent with the O–O bond distance in **4**, and we have observed a good correlation between the O–O stretching frequency and the O–O bond length (Figure 3).¹⁷

The X-band EPR spectrum of $[\text{Co}(\text{13-TMC})(\text{CH}_3\text{CN})]^{2+}$ (**3**) at 4.3 K contains features at $g_\perp = 2.31$ and $g_\parallel \approx 2.07$, which are typical for a low-spin ($S = 1/2$) cobalt(II) species (SI, Figure S8). Complex **4** is EPR silent (X-band, 4.3 K) and exhibits a sharp ^1H NMR spectrum in the 0–10 ppm region (data not shown), indicating that **4** is a low-spin ($S = 0$) cobalt(III) d⁶ species. Taken together, the spectroscopic data with the structural characterization demonstrate that **2** and **4** are low-spin ($S = 0$) cobalt(III)–peroxo complexes with the peroxo ligand bound in a side-on η^2 fashion, $[\text{Co}^{\text{III}}(\text{12-TMC})(\text{O}_2)]^+$ and $[\text{Co}^{\text{III}}(\text{13-TMC})(\text{O}_2)]^+$, respectively.

2.2.4. DFT Calculations. Spin-unrestricted broken symmetry density functional theory (DFT) calculations were performed on the cationic moieties of $[\text{Co}(\text{12-TMC})(\text{O}_2)]^+$ and $[\text{Co}(\text{13-TMC})(\text{O}_2)]^+$, obtained from the crystal structures of **2** and **4**. The relevant bond distances are presented in SI, Table S3. The calculated Co–O, O–O, and average Co–N distances of 1.88, 1.44, and $\sim 2.03\text{ \AA}$, respectively, are in close agreement with the data obtained from X-ray crystallography and Co K-edge EXAFS results for **2**. The DFT

optimized structure of **4** is qualitatively similar to that of **2**, although there is a larger spread in the Co–N distances (see SI, Table S3). This is consistent with the slight decrease in the first shell intensity of the Fourier transform in **4** relative to **2** (see SI, Figure S3 for comparison). The average Co–O and O–O distances are 1.90 and 1.42 \AA , which are in reasonable agreement with the experimental data. The calculated geometric and electronic structures for **2** and **4** are consistent with a low-spin $[\text{Co}(\text{III})\text{--O}_2^{2-}]^+$ ground state as observed from the experimental data.

2.3. Reactivities of Co–O₂ Complexes. **2.3.1. Nucleophilic Reactions.** The reactivity of the cobalt(III)–peroxo complexes was investigated in electrophilic and nucleophilic reactions. First, the electrophilic character of **2** and **4** was tested in the oxidation of thioanisole and cyclohexene. Upon addition of substrates to a solution of **2** and **4** in CH_3CN at 25°C , the intermediate remained intact without showing any absorption spectral change, and product analysis of the reaction solutions revealed that no oxygenated products were formed. These results demonstrate that the Co(III)–peroxo complexes are not capable of conducting electrophilic oxidation with the substrates under the reaction conditions.

The nucleophilic character of **4** was then investigated in aldehyde deformylation, with precedents that metal(III)–peroxo complexes with heme and nonheme ligands react with aldehydes to give corresponding deformylated products.^{4,12a,14} Upon reacting **4** with cyclohexanecarboxaldehyde (CCA) in CH_3CN at 25°C , the characteristic UV–vis absorption bands of **4** disappeared with pseudo-first-order decay (Figure 5a), and product analysis of the reaction solution revealed that cyclohexene ($80 \pm 10\%$) was produced in the oxidation of CCA.^{12a,14,20} The pseudo-first-order fitting of the kinetic data, monitored at 380 nm, yielded the k_{obs} value of $1.6 \times 10^{-2}\text{ s}^{-1}$ (Figure 5a). The pseudo-first-order rate constants increased proportionally with the concentration of CCA, giving a second-order rate constant (k_2) of $2.0 \times 10^{-1}\text{ M}^{-1}\text{ s}^{-1}$ (Figure 5b). Similar results were obtained in the reactions of 2-phenylpropionaldehyde (2-PPA) but with a slower rate ($k_2 = 1.5 \times 10^{-2}\text{ M}^{-1}\text{ s}^{-1}$ at 25°C) (SI, Figure S9). The product analysis of the resulting solution revealed the formation of acetophenone ($90 \pm 10\%$). Activation parameters for the aldehyde deformylation of **4** between 278 and 308 K were determined to be $\Delta H^\ddagger = 64\text{ kJ mol}^{-1}$ and $\Delta S^\ddagger = -67\text{ J mol}^{-1}\text{ K}^{-1}$ for CCA (Figure 5c) and $\Delta H^\ddagger = 62\text{ kJ mol}^{-1}$ and $\Delta S^\ddagger = -77\text{ J mol}^{-1}\text{ K}^{-1}$ for 2-PPA (SI, Figure S9). Further, the reactivity of **4** was investigated with *para*-substituted benzaldehydes, *para*-X–Ph–CHO (X = OMe, Me, F, H), to investigate the effect of *para*-substituents on the benzaldehyde oxidation process by Co(III)–peroxo species. A Hammett plot of the pseudo-first-order rate constants versus σ_p^+ gave a ρ value of 1.7 (Figure S10), which is consistent with the nucleophilic character of the Co-peroxo unit in the oxidation of aldehydes.^{12a} Finally, it is of interest to note that the reactivity of **2** is much lower than that of **4** in nucleophilic reactions; therefore, we were not able to obtain kinetic data for **2** under the reaction conditions. The latter result implies that the nucleophilic character of the peroxo ligand is influenced markedly by the ring size of tetraazamacrocyclic ligands (i.e., $[\text{Co}(\text{13-TMC})(\text{O}_2)]^+ > [\text{Co}(\text{12-TMC})(\text{O}_2)]^+$).

(20) Vaz, A. D. N.; Roberts, E. A.; Coon, M. J. *J. Am. Chem. Soc.* **1991**, *113*, 5886–5887.

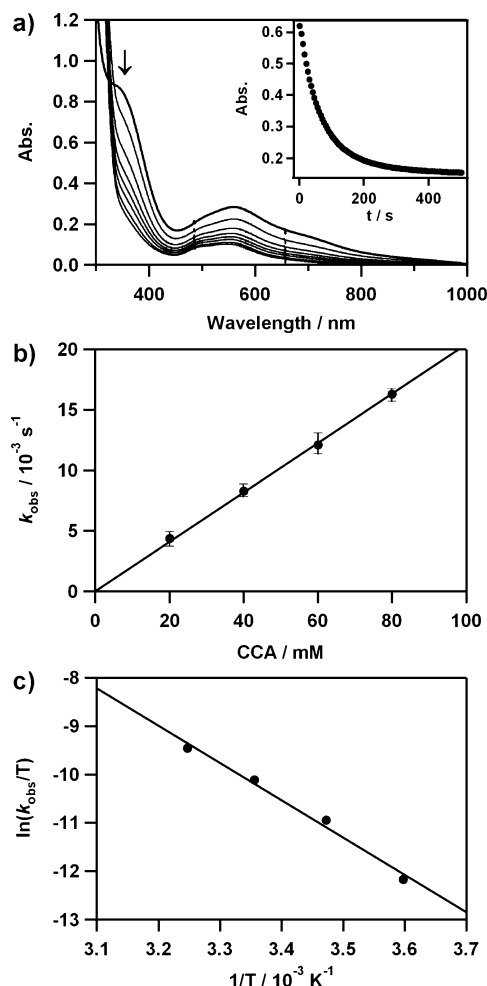
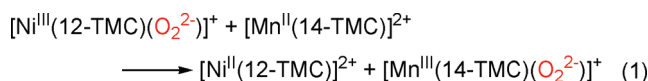


Figure 5. Reactions of $[\text{Co}(\text{13-TMC})(\text{O}_2)]^+$ (**4**) with cyclohexanecarboxaldehyde (CCA) in acetonitrile at 25 °C. (a) UV-vis spectral changes of **4** (2 mM) upon addition of 40 equiv of CCA. Inset shows the time course of the absorbance at 380 nm. (b) Plot of k_{obs} against CCA concentration to determine a second-order rate constant. (c) Plot of first-order rate constants against $1/T$ to determine activation parameters for the reaction of **4** (2 mM) and 30 equiv of CCA.

2.3.2. O₂-Transfer Reactions. It has been shown that a mononuclear Ni(III)–peroxo complex, $[\text{Ni}(\text{12-TMC})(\text{O}_2)]^+$, is capable of transferring the peroxo group to a manganese(II) complex, thus affording the corresponding nickel(II) and manganese(III)–peroxo complexes (eq 1).^{12a} We therefore



attempted the intermolecular dioxygen transfer from the cobalt–peroxo complexes, **2** and **4**, to the $[\text{Mn}(\text{14-TMC})]^{2+}$ complex. Interestingly, addition of $[\text{Mn}(\text{14-TMC})]^{2+}$ to a solution of **2** in CH_3CN at 25 °C resulted in the disappearance of the band ($\lambda_{\text{max}} = 350 \text{ nm}$) corresponding to **2** with the concomitant growth of an absorption band ($\lambda_{\text{max}} = 453 \text{ nm}$) corresponding to $[\text{Mn}(\text{14-TMC})(\text{O}_2)]^+$ (**5**) (Figure 6a).^{14a} The intermolecular O₂-transfer from **2** to $[\text{Mn}(\text{14-TMC})]^{2+}$ was further confirmed by ESI-MS analysis of the reaction solution at different times, where the mass peak at m/z 319.1 corresponding to **2** disappeared with a concomitant appearance of the mass peak at m/z 343.2 corresponding to **5** (Figure 6b). Further, when the O₂-transfer reaction was carried out under

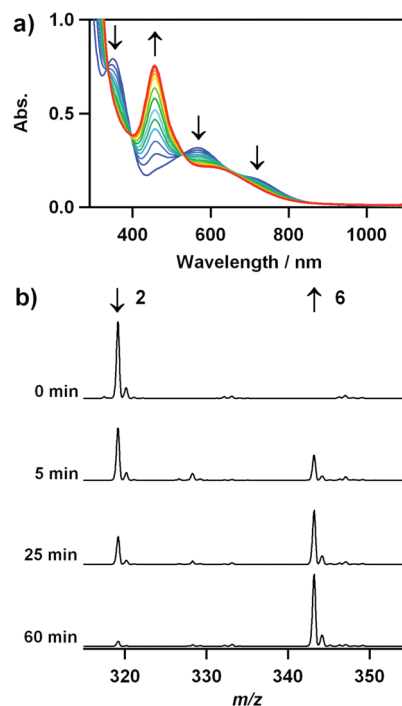
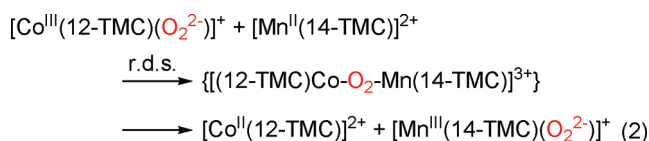


Figure 6. Spectral evidence for O₂-transfer from $[\text{Co}(\text{12-TMC})(\text{O}_2)]^+$ (**2**) to $[\text{Mn}(\text{14-TMC})]^{2+}$. (a) UV-vis spectral changes showing the disappearance of **2** (blue line) and the appearance of $[\text{Mn}(\text{14-TMC})(\text{O}_2)]^+$ (**5**) (red line) upon addition of $[\text{Mn}(\text{14-TMC})]^{2+}$ (2 mM) to a solution of **2** (2 mM) in CH_3CN at 25 °C. (b) ESI-MS changes of **2** at m/z 319.1 and **5** at m/z 343.2 in the reaction of **2** (2 mM) and $[\text{Mn}(\text{14-TMC})]^{2+}$ (2 mM) in CH_3CN at 25 °C.

an ¹⁸O₂ atmosphere, the product **5** did not contain the isotopically labeled ¹⁸O₂ group, demonstrating that molecular oxygen was not involved in the O₂-transfer reaction. Furthermore, we found that the reverse reaction, which is the peroxo ligand transfer from **5** to **2** or **4**, does not occur.

Kinetic studies of the O₂-transfer from **2** to $[\text{Mn}(\text{14-TMC})]^{2+}$ were carried out in acetone at 0 °C (SI, Figure S11a). Addition of 15 equiv of $[\text{Mn}(\text{14-TMC})]^{2+}$ to the solution of **2** yielded a k_{obs} value of $2.2 \times 10^{-3} \text{ s}^{-1}$ under pseudo-first-order conditions. The rate constant increased proportionally with the concentration of $[\text{Mn}(\text{14-TMC})]^{2+}$, giving a second-order rate constant of $k_2 = 1.5 \times 10^{-1} \text{ M}^{-1} \text{ s}^{-1}$ at 0 °C (Figure 7a, red line). The reaction rate was dependent on temperature, and a linear Eyring plot was obtained between 0 and 25 °C to give the activation parameters of $\Delta H^\ddagger = 65 \text{ kJ mol}^{-1}$ and $\Delta S^\ddagger = -63 \text{ J mol}^{-1} \text{ K}^{-1}$ (Figure 7b, red line). The dependence of the rate constants on the concentration of reactants and the significant negative entropy value suggest that the O₂-transfer reaction proceeds via a bimolecular mechanism in which the formation of an undetected $[(\text{12-TMC})\text{Co}-\text{O}_2-\text{Mn}(\text{14-TMC})]^{3+}$ intermediate is the rate-determining step (eq 2). It is of interest to note that the



O₂-transfer from **2** to $[\text{Mn}(\text{14-TMC})]^{2+}$ is ~1100 times slower than that from $[\text{Ni}^{\text{III}}(\text{12-TMC})(\text{O}_2)]^+$ to $[\text{Mn}(\text{14-TMC})]^{2+}$ (e.g., $k_2 = 1.9 \times 10^{-4} \text{ M}^{-1} \text{ s}^{-1}$ for the reaction of **2** and $k_2 = 0.2 \text{ M}^{-1}$

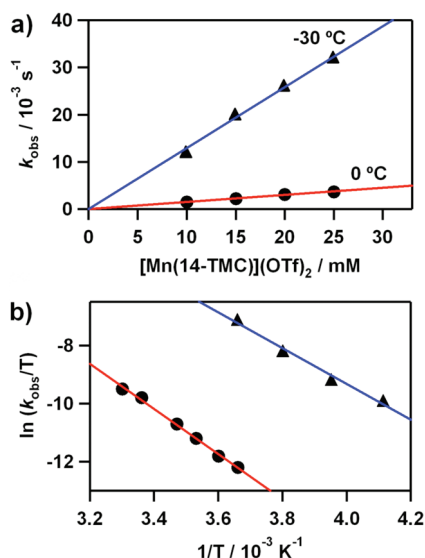


Figure 7. Kinetic studies of O_2 -transfer reactions from $[\text{Co}(\text{12-TMC})(\text{O}_2)]^+$ (**2**) and $[\text{Co}(\text{13-TMC})(\text{O}_2)]^+$ (**4**) to $[\text{Mn}(\text{14-TMC})]^{2+}$. (a) Plots of k_{obs} against the concentration of $[\text{Mn}(\text{14-TMC})]^{2+}$ to determine second-order rate constants for the reactions of **2** at 0°C (red line with \bullet) and **4** at -30°C (blue line with \blacktriangle) in acetone. (b) Plots of first-order rate constants against $1/T$ to determine activation parameters for the reactions of $[\text{Mn}(\text{14-TMC})]^{2+}$ with **2** (1 mM, red line with \bullet) and **4** (1 mM, blue line with \blacktriangle) in acetone.

s^{-1} for the reaction of $[\text{Ni}^{\text{III}}(\text{12-TMC})(\text{O}_2)]^+$ at -50°C ,²¹ indicating that the peroxo group of **2** is much less reactive than that of $[\text{Ni}^{\text{III}}(\text{12-TMC})(\text{O}_2)]^+$ in the attack of the Mn(II) ion (eq 2). The results can be explained by the difference of the enthalpy values of 65 kJ mol^{-1} for **2** and 49 kJ mol^{-1} for $[\text{Ni}^{\text{III}}(\text{12-TMC})(\text{O}_2)]^+$, and the difference of $\Delta\Delta G$ between complexes **2** and $[\text{Ni}^{\text{III}}(\text{12-TMC})(\text{O}_2)]^+$ is $\sim 13\text{ kJ mol}^{-1}$.

To understand the effect of supporting ligands on the O_2 -transfer reaction, we performed kinetic studies with **4** and then compared the reactivities of **2** and **4**. Since the O_2 -transfer from **4** to $[\text{Mn}(\text{14-TMC})]^{2+}$ was fast at 0°C , reactions were carried out in acetone at -30°C . Pseudo-first-order fitting of the kinetic data yielded a k_{obs} value of $1.2 \times 10^{-2}\text{ s}^{-1}$ (SI, Figure S11b). A plot of k_{obs} against the concentration of **4** gave a linear line, affording a second-order rate constant of $k_2 = 1.3\text{ M}^{-1}\text{ s}^{-1}$ at -30°C (Figure 7a, blue line). Activation parameters for the O_2 -transfer from **4** to $[\text{Mn}(\text{14-TMC})]^{2+}$ were determined to be $\Delta H^\ddagger = 51\text{ kJ mol}^{-1}$ and $\Delta S^\ddagger = -71\text{ J mol}^{-1}\text{ K}^{-1}$, by plotting first-order rate constants determined at different temperatures against $1/T$ (Figure 7b, blue line). It is worth noting that the enthalpy value of 51 kJ mol^{-1} for **4** is much smaller than that ($\Delta H^\ddagger = 65\text{ kJ mol}^{-1}$) for **2** and that the difference of $\Delta\Delta G$ between complexes **2** and **4** is $\sim 12\text{ kJ mol}^{-1}$. Consequently, as the ring size of macrocyclic ligands in the cobalt(III)–peroxo complexes increases from 12-TMC to 13-TMC, the O_2 -transfer reaction is facilitated and the reaction rate is enhanced ~ 600 -fold (e.g., $k_2 = 1.9 \times 10^{-4}\text{ M}^{-1}\text{ s}^{-1}$ for **2** and $k_2 = 1.2 \times 10^{-1}\text{ M}^{-1}\text{ s}^{-1}$ for **4** at -50°C).²¹ The results indicate that the peroxo group in **4** is more reactive than that in **2** on the attack of Mn(II) ion in the O_2 -transfer reaction. In addition, the reactivity of **4** is slightly lower than that of $[\text{Ni}^{\text{III}}(\text{12-TMC})(\text{O}_2)]^+$ (e.g., $k_2 = 1.2 \times 10^{-1}\text{ M}^{-1}\text{ s}^{-1}$ for **4** and $k_2 = 2.0 \times 10^{-1}\text{ M}^{-1}\text{ s}^{-1}$ for

$[\text{Ni}^{\text{III}}(\text{12-TMC})(\text{O}_2)]^+$ at -50°C).²¹ Thus, the reactivity order of $[\text{Ni}(\text{12-TMC})(\text{O}_2)]^+ > [\text{Co}(\text{13-TMC})(\text{O}_2)]^+ \gg [\text{Co}(\text{12-TMC})(\text{O}_2)]^+$ is observed in O_2 -transfer reactions.

3. Conclusions

In this study, we synthesized and characterized mononuclear cobalt(III)–peroxo complexes bearing tetraazamacrocyclic ligands, $[\text{Co}^{\text{III}}(\text{12-TMC})(\text{O}_2)]^+$ and $[\text{Co}^{\text{III}}(\text{13-TMC})(\text{O}_2)]^+$. The structural and Co K-edge EXAFS spectroscopic characterization clearly showed that the peroxo ligand is bound in a side-on η^2 fashion. The cobalt(III)–peroxo complexes have shown reactivities in the oxidation of aldehydes and O_2 -transfer reactions. In the aldehyde oxidation reactions, the nucleophilic reactivity of metal(III)–peroxo complexes was found to depend significantly on the ring size of the macrocyclic ligands, with the reactivity order $[\text{Co}(\text{13-TMC})(\text{O}_2)]^+ > [\text{Co}(\text{12-TMC})(\text{O}_2)]^+$. In the O_2 -transfer reactions, the cobalt(III)–peroxo complexes were shown to transfer their peroxo ligand to a manganese(II) complex. The O_2 -transfer reactions were found to depend significantly on the central metal ions and the supporting ligands, showing the reactivity order $[\text{Ni}(\text{12-TMC})(\text{O}_2)]^+ > [\text{Co}(\text{13-TMC})(\text{O}_2)]^+ \gg [\text{Co}(\text{12-TMC})(\text{O}_2)]^+$.

4. Experimental Section

Materials. All chemicals obtained from Aldrich Chemical Co. were of the best available purity and used without further purification unless otherwise indicated. Solvents were dried according to published procedures and distilled under Ar prior to use.²² $\text{H}_2^{18}\text{O}_2$ (90% ^{18}O -enriched, 2% $\text{H}_2^{18}\text{O}_2$ in water) and $^{18}\text{O}_2$ (95% ^{18}O -enriched) were purchased from ICON Services Inc. (Summit, NJ, USA). The 12-TMC and 13-TMC ligands were prepared by reacting an excess amount of formaldehyde and formic acid with 1,4,7,10-tetraazacyclododecane and 1,4,7,10-tetraazacyclotridecane, respectively.²³ All air-sensitive reactions were performed using either a glovebox or standard Schlenk techniques. $[\text{Ni}(\text{12-TMC})(\text{O}_2)]^+$ and $[\text{Mn}(\text{14-TMC})]^{2+}$ were prepared according to the literature methods.^{12a,14a}

Caution. Perchlorate salts are potentially explosive and should be handled with care!

Synthesis of $[\text{Co}(\text{12-TMC})(\text{CH}_3\text{CN})](\text{ClO}_4)_2$. 12-TMC (0.50 g, 2.19 mmol) was added to an acetonitrile solution (50 mL) of $\text{Co}(\text{ClO}_4)_2 \cdot 6\text{H}_2\text{O}$ (0.96 g, 2.63 mmol). The mixture was refluxed for 12 h, giving a reddish brown solution. After the mixture cooled to room temperature, the solvent was then removed under vacuum to give a reddish brown solid, which was collected by filtration and washed with methanol several times to remove the remaining $\text{Co}(\text{ClO}_4)_2 \cdot 6\text{H}_2\text{O}$. Yield: 0.88 g (76%). UV–vis (ϵ , $\text{M}^{-1}\text{ cm}^{-1}$) in CH_3CN : $\sim 332\text{ nm}$ (70), 485 nm (200). ESI-MS (in CH_3CN): m/z 164.0 $[\text{Co}(\text{12-TMC})]^{2+}$. Anal. Calcd for $\text{C}_{14}\text{H}_{31}\text{N}_5\text{O}_8\text{Cl}_2\text{Co}$: C, 31.89; H, 5.93; N, 13.28. Found: C, 31.95; H, 5.90; N, 13.49. X-ray crystallographically suitable crystals were obtained by slow diffusion of diethyl ether into a concentrated acetonitrile solution of $[\text{Co}(\text{12-TMC})(\text{CH}_3\text{CN})](\text{ClO}_4)_2$.

Synthesis of $[\text{Co}(\text{13-TMC})(\text{CH}_3\text{CN})](\text{ClO}_4)_2$. 13-TMC (0.50 g, 2.06 mmol) was added to an acetonitrile solution (50 mL) of $\text{Co}(\text{ClO}_4)_2 \cdot 6\text{H}_2\text{O}$ (0.90 g, 2.47 mmol). The mixture was refluxed for 12 h, affording a violet solution. After the mixture cooled to room temperature, the solvent was removed under vacuum to give a violet solid, which was collected by filtration and then washed with methanol several times to remove the remaining $\text{Co}(\text{ClO}_4)_2 \cdot 6\text{H}_2\text{O}$. Yield: 0.90 g (81%). UV–vis (ϵ , $\text{M}^{-1}\text{ cm}^{-1}$) in CH_3CN : $\sim 345\text{ nm}$ (120), 451 nm (120), 520 nm (150). ESI-MS

(21) Due to the large reactivity difference of the metal–peroxo complexes, the k_2 values were determined at different temperatures and normalized using the Eyring equation.

(22) *Purification of Laboratory Chemicals*; Armarego, W. L. F., Perrin, D. D., Eds.; Pergamon Press: Oxford, 1997.

(23) Halfen, J. A.; Young, V. G., Jr. *Chem. Commun.* **2003**, 2894–2895.

(in CH_3CN): m/z 170.9 $[\text{Co}(\text{13-TMC})]^{2+}$. Anal. Calcd for $\text{C}_{15}\text{H}_{33}\text{N}_5\text{O}_8\text{Cl}_2\text{Co}$: C, 33.28; H, 6.14; N, 12.94. Found: C, 33.25; H, 6.28; N, 12.91. X-ray crystallographically suitable crystals were obtained by slow diffusion of diethyl ether into a concentrated acetonitrile solution of $[\text{Co}(\text{13-TMC})(\text{CH}_3\text{CN})](\text{ClO}_4)_2$.

Synthesis of $[\text{Co}(\text{12-TMC})(\text{O}_2)](\text{ClO}_4)_2$. Aqueous 30% H_2O_2 (28 μL , 0.25 mmol) was added to an acetonitrile solution (5 mL) containing $[\text{Co}(\text{12-TMC})(\text{CH}_3\text{CN})](\text{ClO}_4)_2$ (0.026 g, 0.05 mmol) and triethylamine (14 μL , 0.1 mmol) at -20°C , producing a purple solution. Diethyl ether (20 mL) was added to the resulting solution to yield a purple powder, which was collected by filtration, washed with diethyl ether, and dried in vacuum. Yield: 0.017 g (81%). UV-vis (ϵ , $\text{M}^{-1}\text{cm}^{-1}$) in CH_3CN : 350 nm (450), ~ 500 nm (150), 560 nm (180), ~ 710 nm (90). ESI-MS (in CH_3CN): m/z 319.1 for $[\text{Co}(\text{12-TMC})(^{16}\text{O}_2)]^+$ and m/z 323.1 for $[\text{Co}(\text{12-TMC})(^{18}\text{O}_2)]^+$. $[\text{Co}(\text{12-TMC})(^{18}\text{O}_2)]^+$ was prepared by adding 5 equiv of $\text{H}_2^{18}\text{O}_2$ (16 μL of 90% ^{18}O -enriched, 2% $\text{H}_2^{18}\text{O}_2$ in water) to a solution containing $[\text{Co}(\text{12-TMC})(\text{CH}_3\text{CN})](\text{ClO}_4)_2$ (2 mM) and 2 equiv of triethylamine in CH_3CN (2 mL) at ambient temperature. X-ray crystallographically suitable crystals were obtained by addition of NaBPh_4 .

Synthesis of $[\text{Co}(\text{13-TMC})(\text{O}_2)](\text{ClO}_4)_2$. Aqueous 30% H_2O_2 (28 μL , 0.25 mmol) was added to an acetonitrile solution (5 mL) containing $[\text{Co}(\text{13-TMC})(\text{CH}_3\text{CN})](\text{ClO}_4)_2$ (0.027 g, 0.05 mmol) and triethylamine (14 μL , 0.1 mmol) at -20°C , producing a purple solution. Diethyl ether (20 mL) was added to the resulting solution to yield a purple powder, which was collected by filtration, washed with diethyl ether, and dried in vacuum. Yield: 0.013 (60%). UV-vis (ϵ , $\text{M}^{-1}\text{cm}^{-1}$) in CH_3CN : 348 nm (620), ~ 500 nm (170), 562 nm (210), ~ 710 nm (100). ESI-MS (in CH_3CN): m/z 333.1 for $[\text{Co}(\text{13-TMC})(^{16}\text{O}_2)]^+$ and m/z 337.1 for $[\text{Co}(\text{13-TMC})(^{18}\text{O}_2)]^+$. $[\text{Co}(\text{13-TMC})(^{18}\text{O}_2)]^+$ was prepared by adding 5 equiv of $\text{H}_2^{18}\text{O}_2$ (16 μL of 90% ^{18}O -enriched, 2% $\text{H}_2^{18}\text{O}_2$ in water) to a solution containing $[\text{Co}(\text{13-TMC})(\text{CH}_3\text{CN})](\text{ClO}_4)_2$ (2 mM) and 2 equiv of triethylamine in CH_3CN (2 mL) at ambient temperature. X-ray crystallographically suitable crystals were obtained by slow diffusion of diethyl ether into a concentrated acetonitrile solution of $[\text{Co}(\text{13-TMC})(\text{O}_2)](\text{ClO}_4)_2$.

Reactivity Studies. All reactions were run in a 1-cm UV cuvette by monitoring the UV-vis spectral changes of the reaction solutions, and rate constants were determined by fitting the changes in absorbance at 562 nm for $[\text{Co}(\text{13-TMC})(\text{O}_2)]^+$. Reactions were run at least in triplicate, and the data reported represent the average of these reactions. $[\text{Co}(\text{13-TMC})(\text{O}_2)]^+$ was prepared by reacting $[\text{Co}(\text{13-TMC})(\text{CH}_3\text{CN})]^+$ with 5 equiv of H_2O_2 in the presence of 2 equiv of TEA. The intermediate $[\text{Co}(\text{13-TMC})(\text{O}_2)]^+$ (2 mM) was then used in reactivity studies, such as the oxidation of cyclohexanecarboxaldehyde (CCA) and 2-phenylpropionaldehyde (2-PPA) at 25°C . The purity of substrates was checked by GC and GC-MS prior to use. After completion of the reactions, products were analyzed by injecting reaction solutions directly into the GC and GC-MS instruments. Products were identified by comparison with authentic samples, and product yields were determined by comparison against standard curves prepared with authentic samples and using decane as an internal standard.

The O_2 -transfer reactions were carried out by adding appropriate amounts of $[\text{Mn}(\text{14-TMC})]^{2+}$ to a solution of $[\text{Co}(\text{12-TMC})(\text{O}_2)]^+$ (1 mM) and $[\text{Co}(\text{13-TMC})(\text{O}_2)]^+$ (1 mM), prepared with isolated cobalt-peroxo complexes in acetone. All reactions were run in a 1-cm UV cuvette by monitoring the UV-vis spectral changes of the reaction solutions, and rate constants were determined by fitting the changes in absorbance at 453 nm. The O_2 -transfer reactions were further confirmed by ESI-MS analysis of the reaction solutions.

Physical Methods. UV-vis spectra were recorded on a Hewlett-Packard 8453 diode array spectrophotometer equipped with a UNISOKU Scientific Instruments for low-temperature experiments or with a circulating water bath. Electrospray ionization mass spectra were collected on a Thermo Finnigan (San Jose, CA, USA) LCQ@ Advantage MAX quadrupole ion trap instrument, by infusing

samples directly into the source using a manual method. The spray voltage was set at 4.2 kV, and the capillary temperature at 80°C . Resonance Raman spectra were obtained using a liquid nitrogen cooled CCD detector (CCD-1024 \times 256-OPEN-1LS, HORIBA Jobin Yvon) attached to a 1-m single polychromator (MC-100DG, Ritsu Oyo Kogaku) with a 1200 grooves/mm holographic grating. An excitation wavelength of 441.6 nm was provided by a He-Cd laser (Kimmion Koha, IK5651R-G and KR1801C), with 15 mW of power at the sample point. All measurements were carried out with a spinning cell (1000 rpm) at 0°C . Raman shifts were calibrated with indene, and the accuracy of the peak positions of the Raman bands was $\pm 1\text{ cm}^{-1}$. EPR spectra were taken at 4 K using a X-band Bruker EMX-plus spectrometer equipped with a dual mode cavity (ER 4116DM). Low temperatures were achieved and controlled with an Oxford Instruments ESR900 liquid He quartz cryostat with an Oxford Instruments ITC503 temperature and gas flow controller. EPR spectra were obtained on a JEOL JES-FA200 spectrometer. ^1H NMR spectra were measured with Bruker model digital AVANCE III 400 FT-NMR spectrometer. The effective magnetic moments were determined using the modified ^1H NMR method of Evans at room temperature.²⁴ A WILMAD coaxial insert (sealed capillary) tube containing the blank acetonitrile- d_3 solvent (with 1.0% TMS) only was inserted into the normal NMR tubes containing the complexes (8 mM) dissolved in acetonitrile- d_3 (with 0.05% TMS). The chemical shift of the TMS peak (and/or solvent peak) in the presence of the paramagnetic metal complexes was compared to that of the TMS peak (and/or solvent peak) in the inner coaxial insert tube. The effective magnetic moment was calculated using the equation $\mu = 0.0618(\Delta\nu T/2fM)^{1/2}$, where f is the oscillator frequency (MHz) of the superconducting spectrometer, T is the absolute temperature, M is the molar concentration of the metal ion, and $\Delta\nu$ is the difference in frequency (Hz) between the two reference signals.^{24c} Crystallographic analysis was conducted with a SMART APEX CCD equipped with a Mo X-ray tube at the Crystallographic Laboratory of Ewha Womans University.

X-ray Crystallography. Single crystals of **1**-(ClO_4)₂, **2**-(BPh_4) $\cdot\text{CH}_3\text{CN}$, **3**-(ClO_4)₂, and **4**-(ClO_4) $\cdot\text{CH}_3\text{CN}$ were picked from solutions by a nylon loop (Hampton Research Co.) on a handmade cooper plate mounted inside a liquid N_2 Dewar vessel at $ca. -40^\circ\text{C}$ and mounted on a goniometer head in a N_2 cryostream. Data collections were carried out on a Bruker SMART AXS diffractometer equipped with a monochromator in the Mo $\text{K}\alpha$ ($\lambda = 0.71073\text{ \AA}$) incident beam. The CCD data were integrated and scaled using the Bruker-SAINT software package, and the structure was solved and refined using SHELXTL V 6.12.²⁵ Hydrogen atoms were located in the calculated positions for **2**-(BPh_4) $\cdot\text{CH}_3\text{CN}$ and **4**-(ClO_4) $\cdot\text{CH}_3\text{CN}$. Due to the high degree of disorder, however, hydrogen atoms could not be placed in ideal positions for **3**-(ClO_4)₂ and the coordinated CH_3CN of **1**-(ClO_4)₂. Crystal data for **1**-(ClO_4)₂: $\text{C}_{14}\text{Cl}_2\text{CoN}_5\text{O}_8$, Orthorhombic, $Pnma$, $Z = 4$, $a = 14.718(2)\text{ \AA}$, $b = 8.9472(12)\text{ \AA}$, $c = 17.545(2)\text{ \AA}$, $V = 2310.4(5)\text{ \AA}^3$, $\mu = 1.022\text{ mm}^{-1}$, $\rho_{\text{calc}} = 1.507\text{ g/cm}^3$, $R_1 = 0.0794$, $wR_2 = 0.2227$ for 2927 unique reflections, 160 variables. Crystal data for **2**-(BPh_4) $\cdot\text{CH}_3\text{CN}$: $\text{C}_{38}\text{H}_{51}\text{CoBN}_5\text{O}_2$, Monoclinic, $P2(1)/c$, $Z = 4$, $a = 12.2417(15)\text{ \AA}$, $b = 27.912(3)\text{ \AA}$, $c = 11.1477(13)\text{ \AA}$, $\beta = 110.063(2)^\circ$, $V = 3577.9(7)\text{ \AA}^3$, $\mu = 0.520\text{ mm}^{-1}$, $\rho_{\text{calc}} = 1.262\text{ g/cm}^3$, $R_1 = 0.0365$, $wR_2 = 0.0523$ for 8229 unique reflections, 429 variables. Crystal data for **3**-(ClO_4)₂: $\text{C}_{15}\text{Cl}_2\text{CoN}_5\text{O}_8$, Tetragonal, $P4/nmm$, $Z = 2$, $a = 9.2584(6)\text{ \AA}$, $b = 9.2584(6)\text{ \AA}$, $c = 14.1473(17)\text{ \AA}$, $V = 1212.68(18)\text{ \AA}^3$, $\mu = 0.972\text{ mm}^{-1}$, $\rho_{\text{calc}} = 1.391\text{ g/cm}^3$, $R_1 = 0.0673$, $wR_2 = 0.1807$ for 890 unique reflections, 75 variables. Crystal data for **4**-(ClO_4) $\cdot\text{CH}_3\text{CN}$: $\text{C}_{15}\text{H}_{33}\text{ClCoN}_5\text{O}_6$, Orthorhombic, $Pca2(1)$, $Z = 4$, $a = 12.789(3)\text{ \AA}$, $b = 9.5673(18)\text{ \AA}$, $c = 17.218(3)\text{ \AA}$, $V = 2106.7(7)\text{ \AA}^3$, $\mu = 0.982\text{ mm}^{-1}$, $\rho_{\text{calc}} =$

- (24) (a) Evans, D. F. *J. Chem. Soc.* **1959**, 2003–2005. (b) Löliger, J.; Scheffold, R. *J. Chem. Educ.* **1972**, 49, 646–647. (c) Evans, D. F.; Jakubovic, D. A. *J. Chem. Soc., Dalton Trans.* **1988**, 2927–2933. (25) Sheldrick, G. M. *SHELXTL/PC*, version 6.12 for Windows XP; Bruker AXS Inc.: Madison, Wisconsin, USA, 2001.

Table 2. Crystallographic Data and Structure Refinements for **1**-(ClO₄)₂, **2**-(BPh₄)·CH₃CN, **3**-(ClO₄)₂, and **4**-(ClO₄)·CH₃CN

	1 -(ClO ₄) ₂	2 -(BPh ₄)·CH ₃ CN	3 -(ClO ₄) ₂	4 -(ClO ₄)·CH ₃ CN
Empirical formula	C ₁₄ H ₂₈ Cl ₂ CoN ₅ O ₈	C ₃₈ H ₅₁ CoBN ₅ O ₂	C ₁₅ Cl ₂ CoN ₅ O ₈	C ₁₅ H ₃₃ ClCoN ₅ O ₆
Formula weight	524.24	679.58	508.03	473.84
Temperature (K)	298(2)	170(2)	298(2)	170(2)
Wavelength (Å)	0.71073	0.71073	0.71073	0.71073
Crystal system	orthorhombic	monoclinic	tetragonal	orthorhombic
Space group	<i>Pnma</i>	<i>P2(1)/c</i>	<i>P4/nmm</i>	<i>Pca2(1)</i>
Unit cell dimensions				
<i>a</i> (Å)	14.718(2)	12.2417(15)	9.2584(6)	12.789(3)
<i>b</i> (Å)	8.9472(12)	27.912(3)	9.2584(6)	9.5673(18)
<i>c</i> (Å)	17.545(2)	11.1477(13)	14.1473(17)	17.218(3)
α (deg)	90.00	90.00	90.00	90.00
β (deg)	90.00	110.063(2)	90.00	90.00
γ (deg)	90.00	90.00	90.00	90.00
Volume (Å ³)	2310.4(5)	3577.9(7)	1212.68(18)	2106.7(7)
<i>Z</i>	4	4	2	4
<i>d</i> _{calcd} (g/cm ^{−3})	1.507	1.262	1.391	1.494
μ (mm ^{−1})	1.022	0.520	0.972	0.982
Reflections collected	13 894	21 911	7455	22 983
Independent reflections [<i>R</i> (int)]	2927 [0.0966]	8229 [0.0688]	890 [0.0587]	3632 [0.0352]
Parameters	160	429	75	258
Goodness-of-fit on <i>F</i> ²	1.030	0.960	1.065	1.003
Final <i>R</i> [<i>I</i> > 2 σ (<i>I</i>)]	0.0794	0.0365	0.0673	0.0345
Final <i>wR</i> [<i>I</i> > 2 σ (<i>I</i>)]	0.2227	0.0481	0.1745	0.1164

1.494 g/cm³, *R*₁ = 0.0345, *wR*₂ = 0.1164 for 3632 unique reflections, 258 variables. The crystallographic data for **1**-(ClO₄)₂, **2**-(BPh₄)·CH₃CN, **3**-(ClO₄)₂, and **4**-(ClO₄)·CH₃CN are listed in Table 2, and Tables 1 and S1 list the selected bond distances and angles. CCDC-744572 for **1**-(ClO₄)₂, -744571 for **2**-(BPh₄)·CH₃CN, -744573 for **3**-(ClO₄)₂ and -778131 for **4**-(ClO₄)·CH₃CN contain the supplementary crystallographic data for this paper. These data can be obtained free of charge via www.ccdc.cam.ac.uk/data_request/cif (or from the Cambridge Crystallographic Data Centre, 12, Union Road, Cambridge CB2 1EZ, UK; fax: (+44) 1223-336-033; or deposit@ccdc.cam.ac.uk).

X-ray Absorption Spectroscopy. The Co K-edge X-ray absorption spectra of **2** and **4** were measured at the Stanford Synchrotron Radiation Laboratory (SSRL) on the focused 16-pole 2.0 T wiggler beamline 9-3 under standard ring conditions of 3 GeV and 80–100 mA. A Si(220) double crystal monochromator was used for energy selection. A Rh-coated harmonic rejection mirror and a cylindrical Rh-coated bent focusing mirror were used. The solution samples for **2** and **4** (5 mM in Co and ~120 μ L) were transferred into 2-mm delrin XAS cells with 37- μ m Kapton tape windows at −20 °C. The samples were immediately frozen after preparation and stored under liquid N₂. During data collection, the samples were maintained at a constant temperature of ~10–15 K using an Oxford Instruments CF 1208 liquid helium cryostat. Data were measured to *k* = 14 Å^{−1} in fluorescence mode by using a Canberra Ge 30-element array detector. Internal energy calibration was accomplished by simultaneous measurement of the absorption of a Co-foil placed between two ionization chambers situated after the sample. The first inflection point of the foil spectrum was fixed at 7709.5 eV. Data presented here are 8-scan average spectra for both **2** and **4**, which were processed by fitting a second-order polynomial to the pre-edge region and subtracting this from the entire spectrum as background. A four-region spline of orders 2, 3, 3, and 3 was used to model the smoothly decaying post-edge region. The data were normalized by subtracting the cubic spline and assigning the edge jump to 1.0 at 7725 eV using the Pyspline program.²⁶

Theoretical EXAFS signals $\chi(k)$ were calculated by using *FEFF* (macintosh version 8.4)^{27–29} and the crystal structures of **2** and **4**.

The theoretical models were fit to the data using EXAFSPAK.³⁰ The structural parameters that varied during the fitting process were the bond distance (*R*) and the bond variance σ^2 , which is related to the Debye–Waller factor resulting from thermal motion, and the static disorder of the absorbing and scattering atoms. The non-structural parameter *E*₀ (the energy at which *k* = 0) was also allowed to vary but was restricted to a common value for every component in a given fit. Coordination numbers were systematically varied in the course of the fit but were fixed within a given fit.

Electronic Structure Calculations. Gradient-corrected, (GGA) spin-unrestricted, broken-symmetry, density functional calculations were carried out using the ORCA^{31,32} package on an 8-CPU linux cluster. The Becke88^{33,34} exchange and Perdew86³⁵ correlation nonlocal functionals were employed to compare the geometric and electronic structure differences between **2** and **4**. The coordinates obtained from the crystal structure of **2** and **4** were used as the starting input structure. The core properties basis set CP(PPP)^{32,36} (as implemented in ORCA) was used on Co, and the Ahlrichs' all electron triple- ζ TZVP^{37,38} basis set was used on all other atoms. The calculations were performed in a dielectric continuum using the conductor-like screening model (COSMO). Acetonitrile was chosen as the dielectric material. Population analyses were performed by means of Mulliken Population Analysis (MPA). Compositions of molecular orbitals and overlap populations between molecular fragments were calculated using QMForge.²⁶

Acknowledgment. The research was supported by NRF/MEST of Korea through the CRI, WCU (R31-2008-000-10010-0), and GRL (2010-00353) Programs (W.N.), the Ministry of Education,

(26) Tenderholt, A. *Pyspline and QMForge*; 2007.

(27) Rehr, J. J.; Albers, R. C. *Rev. Mod. Phys.* **2000**, *72*, 621–654.

(28) Rehr, J. J.; Mustre de Leon, J.; Zabinsky, S. I.; Albers, R. C. *J. Am. Chem. Soc.* **1991**, *113*, 5135–5140.

(29) Mustre de Leon, J.; Rehr, J. J.; Zabinsky, S. I.; Albers, R. C. *Phys. Rev. B* **1991**, *44*, 4146–4156.

(30) George, G. N. *EXAFSPAK and EDG-FIT*; 2000.

(31) Neese, F. *ORCA: An ab Initio, DFT and Semiempirical Electronic Structure Package*, version 2.4, revision 16; 2004.

(32) Neese, F.; Olbrich, G. *Chem. Phys. Lett.* **2002**, *362*, 170–178.

(33) Becke, A. D. *Phys. Rev. A* **1988**, *38*, 3098–3100.

(34) Becke, A. D. *J. Chem. Phys.* **1993**, *98*, 5648–5652.

(35) Perdew, J. P. *Phys. Rev. B* **1986**, *33*, 8822–8824.

(36) Sinnacker, S.; Slep, L. D.; Bill, E.; Neese, F. *Inorg. Chem.* **2005**, *44*, 2245–2254.

(37) Schaefer, A.; Horn, H.; Ahlrichs, R. *J. Chem. Phys.* **1992**, *97*, 2571–2577.

(38) Schaefer, A.; Huber, C.; Ahlrichs, R. *J. Chem. Phys.* **1994**, *100*, 5829–5835.

Culture, Sports, Science and Technology of Japan through the Global COE program and Priority Area (No. 20050029) (T.O.), and NIH Grant DK-31450 (E.I.S.). SSRL operations are funded by the Department of Energy, Office of Basic Energy Sciences. The SSRL Structural Molecular Biology program is supported by the National Institutes of Health, National Center for Research Resources, Biomedical Technology Program, and the Department of Energy, Office of Biological and Environmental Research. This publication was made possible by Award P41 RR001209 from the National Center for Research Resources (NCRR), a component of the National Institutes of Health (NIH).

Supporting Information Available: Non-phase-shift-corrected Fourier transform data, their corresponding EXAFS data, and *FEFF* best fit parameters for **2** and **4**. X-ray crystal structures of **1** and **3**, resonance Raman data of **2** and **4**, EPR data of **1–4**, COSY NMR spectrum of **2**, kinetic data of the reactions of **4** with 2-PPA and *para*-X-Ph-CHO, UV-vis spectral changes of the O₂-transfer reactions of **2** and **4**, and X-ray crystallographic files of **1–4** in CIF format. This material is available free of charge via the Internet at <http://pubs.acs.org>.

JA107177M